Journal of Materials Chemistry A

PAPER

View Article Online
View Journal | View Issue

Cite this: J. Mater. Chem. A, 2019, 7, 10523

Microbelt–void–microbelt-structured SnO_2@C as an advanced electrode with outstanding rate capability and high reversibility†

Wenhe Xie,[ab] Qishang Wang,[ab] Junqi Xu,[*ab] Yang Yu,[ab] Ru Zhao,[ab] Na Li,[ab] Menghui Li,[ab] Yifan Du,[ab] Shanglong Peng[*c] and Guozhong Cao[*d]

Received 15th January 2019
Accepted 26th March 2019

DOI: 10.1039/c9ta00527g

rsc.li/materials-a

Nanoscale SnO_2 materials are highly active in charge/discharge processes, but suffer from both poor interconnectivity and re-agglomeration. In this paper, we report the development of a novel microbelt–void–microbelt SnO_2@C structure, in which the inner SnO_2 nanoparticles-derived microbelt possessed the advantage of high reactivity, the abundant void space effectively buffered the volume change, and the outer microscale carbon shell supplied a fast convenient electronic conduction path and shortened the ion-diffusion distance. Resultant microbelt–void–microbelt-structured SnO_2@C-based half cells delivered a high capacity of 1227 mA h g^{-1} after 300 cycles at 300 mA g^{-1}, and a superior rate performance of 509 mA h g^{-1} at a high current density of 10 A g^{-1}. The full-cell measurements coupling with $LiCoO_2$ showed a high capacity of 588 mA h g^{-1} after 100 cycles. The superior electrochemical performance may be attributed to the unique microbelt–void–microbelt structure, which enables highly reversible alloying and allows the conversion reaction of SnO_2 to Sn in the long-term cyclic processes.

1. Introduction

Lithium-ion batteries (LIBs) dominate the electrochemical energy storage markets due to their significant advantages, such as long cycle life and high energy density,[1–8] which are critical indicators to value battery performance.[9–11] Unfortunately, the energy density of LIBs has hardly increased in the past few years. One key factor is the current commercial graphite anode, which possesses a quite low theoretical specific capacity of 372 mA h g^{-1}, and thus, there is an urgent and reasonable need to explore novel anode materials with a higher theoretical specific capacity to meet the increasingly demanding requirements.[11–29]

As a competitive candidate for anodes, SnO_2 has attracted persistent attention due to its nature abundance, high theoretical specific capacity, and low working potential.[30–35] Despite these tempting advantages, conventional bulk SnO_2 materials suffer from serious particle fracture and loose electrical contact with the current collector, originating from the huge volume inflation (about 360%) that occurs in charge/discharge processes. Because of the insufficient reaction with lithium ions, SnO_2 has long been identified as an alloy-type anode material for LIBs.[36–42] In other words, the conversion process of SnO_2 to Sn is irreversible, and only the Sn alloying reaction is reversible, and thus the delivering theoretical capacity is only 780 mA h g^{-1}. Recently, various SnO_2 nanostructures, including nanospheres,[43–45] nanowires,[46,47] nanotubes,[48,49] and nanosheets,[50,51] have been engineered as anode materials, and it has been shown that these nano-design strategies not only buffer the volume changes but also improve the electrochemical activity. Also, the measured capacity is usually much higher than 780 mA h g^{-1}, likely resulting from the reversible reaction of SnO_2 to Sn.[22,52,53]

Although nano-design methods can improve the electrochemical performance in the initial cyclic processes, SnO_2 nanomaterial-based electrodes still face the challenge of pulverization and re-agglomeration. These difficulties lead to a rapid capacity decay in long-term cycle processes because the large volume inflation can destroy the electrode. Numerous efforts have been made to tackle the above-mentioned difficulties. One of the most promising approaches is to build a yolk–shell structure,[54] in which void space is introduced to buffer the active material volume changes. For example, Kang *et al.* prepared yolk–shell-structured SnO_2 powder as an anode material for LIBs, where it exhibited a capacity of 642 mA h g^{-1} at 625 mA g^{-1} after 40 cycles,[55] whereas the densely structured spherical SnO_2 delivered a much lower capacity of 294 mA h g^{-1} under the same conditions. Zhao *et al.* synthesized SnO_2@C

[a]Key Laboratory of Microelectronics and Energy of Henan Province, Xinyang Normal University, Xinyang 464000, PR Chin. E-mail: phxujunqi@126.com

[b]Energy-Saving Building Materials Innovative Collaboration Center of Henan Province, Xinyang Normal University, Xinyang 464000, PR China

[c]School of Physical Science and Technology, Lanzhou University, Lanzhou 730000, PR. China. E-mail: pengshl@lzu.edu.cn

[d]Department of Materials Science and Engineering, University of Washington, Seattle, USA. E-mail: gzcao@u.washington.edu

† Electronic supplementary information (ESI) available. See DOI: 10.1039/c9ta00527g

yolk–shell nanospheres *via* through a two-step sol–gel coating process,[56] which, when applied as an electrode, the materials delivered a high reversible capacity of 630 mA h g^{-1} after 100 cycles at 100 mA g^{-1}. For comparison, the pure hollow SnO_2 particles faded quickly to a low value of only 52 mA h g^{-1} after 70 cycles. Due to the void providing the space for the inflation from the active materials in the charge/discharge process, nanostructures can facilitate the cycle stability and enhance the electrochemical performance.[57–61] However, their cycle and rate performance are still not ideal because the nanoscale electrode materials tend to suffer from poor interconnectivity and poor conductivity. In view of such problems, linking these yolk–shell structures together may be an effective method to enhance the interconnectivity (conductivity), and thus could further improve the electrochemical performance.

In this work, a novel microbelt–void–microbelt structured SnO_2@C was successfully prepared for the first time. The scheme of the synthesis process is illustrated in Fig. 1. First, the SnO_2 nanoparticles formed microbelts as fabricated by a facile electrospinning technology. Then the microbelt–void–microbelt SnO_2@C structure was fabricated *via* a template approach. Compared with the conventional yolk–shell nanospheres or nanopowders, the present microbelt–void–microbelt-structured SnO_2@C has several significant advantages: (1) the outer micro-scale carbon shell possesses nanoscale thickness, which shortens the lithium-ion-diffusion distance and favors fast electronic conduction; (2) the inner microbelt consists of numerous cross-linked SnO_2 nanoparticles, which gives SnO_2 high reactivity with lithium ions; (3) due to the existence of the void space, the volume inflation of active SnO_2 microbelts can be confined in the nanoscale thickness of the carbon shell, which, thus, perfectly solves the volume inflation problem. These measurements greatly improve the electrode kinetics and promote a highly reversible reaction process in the long-term cyclic process. A fabricated microbelt–void–microbelt SnO_2@C half cell showed a high capacity of 1227 mA h g^{-1} after 300 cycles at 300 mA g^{-1}, and a superior rate performance of 509 mA h g^{-1} at 10 A g^{-1}. The full-cell test exhibited a reversible capacity of 588 mA h g^{-1} after 100 cycles.

2. Experimental

2.1 Preparation of SnO_2 microbelts

The SnO_2 microbelts were fabricated *via* a facile electrospinning approach. To prepare the electrospinning precursor solution, 10 mL *N*,*N*-dimethylformamide (DMF) and 1.8 g polyvinylpyrrolidone (PVP, $M_w = 1\,300\,000$, purchased from Sigma-Aldrich Corporation) were mixed and stirred to form a uniform solution. Next, 1.0 g $SnCl_2 \cdot 2H_2O$ was added in the mixture with continuous magnetic stirring for about 10 h. Then, the precursor solution was applied on electrospinning equipment (WL-2, Beijing Aibo Zhiye Ion Technology Limited Company, China). The inner diameter of the syringe needle was about 0.5 mm, and the solution pump speed was 2.5 mL h^{-1}. The applied voltage was about 13.5 kV and the distance from the needle to grounded aluminum foil was 15 cm. Notably, the electrospinning environment temperature was controlled at about 50 °C. The belt formation process can be divided into three parts: first, the jet containing DMF, $SnCl_2$, and PVP was ejected under the action of a high-voltage electric field. Second, DMF solvent quickly evaporated in the air, while the PVP polymer and $SnCl_2$ were left on the surface of the jet. Finally the formed $SnCl_2$/PVP tubes collapsed into the belt under the huge pressure gap between the outer high atmospheric pressure and the inner low gas pressure of the tubes.[62,63] Finally, the electrospinning products were calcined in a muffle furnace at 500 °C for 4 h in the air.

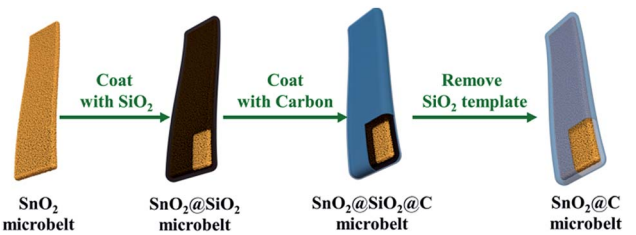

Fig. 1 Schematic illustration of the formation process of microbelt–void–microbelt structured SnO_2@C.

2.2 Preparation of microbelt–void–microbelt structured SnO_2@C

First, 100 mg of as-prepared SnO_2 microbelts and 150 mg PVP were dispersed in a mixture solution containing 10 mL deionized water, 80 mL ethanol, and 2 mL ammonia water. Then, 3 mL tetraethyl orthosilicate (TEOS) was added drop-wise for 2 h with moderate magnetic stirring, and the resulting SnO_2@SiO_2 sample was collected by centrifugation. Later, the SnO_2@SiO_2 was dispersed in dopamine hydrochloride and tris-buffer solution.[64–66] The SnO_2@SiO_2@ polydopamine microbelts were centrifuged and carbonized in an argon atmosphere at 600 °C for 4 h. The microbelt–void–microbelt-structured SnO_2@C was finally prepared after removing the SiO_2 template using 10% wt HF solution.

2.3 Characterization

The morphologies of the samples were observed by field-emission scanning electron microscopy (FESEM, S-4800, Hitachi) and transmission electron microscopy (TEM, Tecnai G^2 F20, FEI). The material structure and composition were identified by X-ray diffraction (XRD, Rigaku D/Max-2400 diffractometer, Cu Kα radiation) and X-ray photoelectron spectroscopy (XPS, Kratos AXIS Ultra DLD, Al Kα probe beam). Thermogravimetric analysis (TGA) of the microbelt–void–microbelt-structured SnO_2@C sample was conducted under an air atmosphere, and the temperature heating rate was 5 °C min^{-1} in the range from 50 °C to 800 °C.

2.4 Cell assembling and electrochemical analysis

To prepare the anode working electrodes, 80 mg of microbelt–void–microbelt-structured SnO_2@C or SnO_2 microbelts and 10 mg acetylene black were fully ground, and 10 mg sodium alginate was dissolved in deionized water to form a uniform

binder solution. Then, the active material, conductive agent, and binder solution were mixed to get a thick slurry, which was cast on a commercial copper foil and dried in a vacuum oven. After that, the copper foil was cut into 12 mm wafers by a slicing machine; the active mass loading was about 0.8–2 mg cm^{-2}. The specific capacity of the present microbelt–void–microbelt-structured SnO_2@C was measured based on the weight of the overall material. The $LiCoO_2$ cathode electrode was prepared using a similar slurry method, while the corresponding binder and current collector were PVDF and commercial aluminum foil, respectively. Both the half- and full-cells were assembled in an argon-filled glove box (H_2O, O_2 < 0.1 ppm, Etelux) using CR 2032 coin cells, and Whatman GF/F-90 glass fibers as the separators, while the organic electrolyte was 1 M $LiPF_6$ dissolved in ethylene carbonate (EC) and dimethyl carbonate (DEC) mixture with a volume ratio of 1 : 1. The half cells consisted of a SnO_2-based anode working electrode and lithium foil counter electrode. For the full-cells, the lithium foil counter electrode was replaced by the prepared $LiCoO_2$ cathode. The assembled cells were tested on a multi-channel battery tester channel (Neware, BTS-610) and electrochemical workstation (CHI-660E). Electrochemical impedance spectroscopy (EIS) measurements were carried out in the frequency range of 0.01–100 000 Hz with an applied perturbation voltage of 5 mV.

3. Results and discussion

The formation process of the microbelt–void–microbelt-structured SnO_2@C is described in the Experimental section. The morphologies of the intermediate products, including the initial electrospinning sample, SnO_2 microbelts, and SnO_2@-SiO_2@C microbelts, were characterized and the results shown in Fig. S1, S2 and S3 (ESI),† respectively.

The composition and structure of the obtained SnO_2 microbelts (blue curve) and microbelt–void–microbelt-structured SnO_2@C (navy curve) were characterized by X-ray diffraction (XRD), as shown in Fig. 2a. All the peaks of the SnO_2 microbelts were in good agreement with the rutile SnO_2 (JCPDS card no. 41-1445) from both curves. In addition to the rutile SnO_2 peaks, a broad peak centered at about 23° could also be found from the microbelt–void–microbelt-structured SnO_2@C sample (navy curve), which was caused by the amorphous carbon from the carbonization of polydopamine. No diffraction peaks of Sn or SnO were found, which proves that the SiO_2 template effectively avoided SnO_2 being reduced by carbon because this design could successfully prevent direct contact between the tin oxide and carbon. The XPS spectra in Fig. 2b and c demonstrated the existence of Sn, O, C, and N elements after carbon coating, where the C and N originate from the carbonized polydopamine. From the TGA profile (as shown in Fig. 2d), we can see that the mass weight of the microbelt–void–microbelt-structured SnO_2@C sample was significantly reduced at 300–580 °C. The reduced weight (about 18 wt%) could be attributed to the fact that the outer carbon material was oxidized and decomposed in air. The TGA measurement showed that the mass rate of carbon content and SnO_2 were about 18 and 82 wt%, respectively.

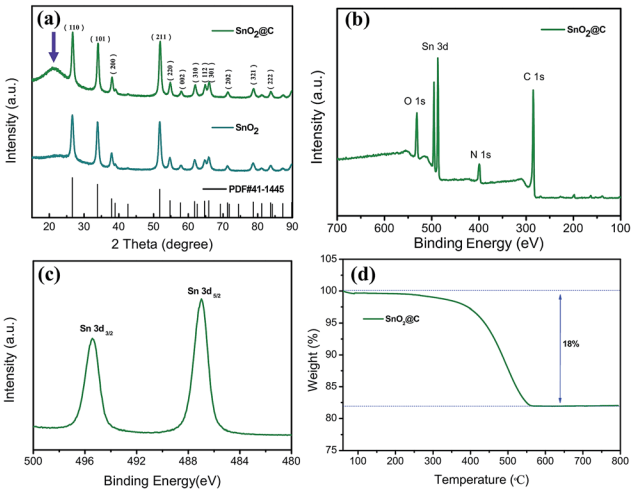

Fig. 2 (a) XRD patterns of microbelt–void–microbelt-structured SnO_2@C and pure SnO_2 microbelts. (b) Full XPS spectrum and (c) high-resolution Sn 3d XPS spectrum of microbelt–void–microbelt-structured SnO_2@C. (d) TGA profile of the microbelt–void–microbelt-structured SnO_2@C.

The detail morphologies of the prepared microbelt–void–microbelt-structured SnO_2@C were also examined by SEM and TEM, as shown in Fig. 3. As expected, the sample still presented a typical belt structure (width about 1 micron) as recorded by the SEM images in Fig. 3a and b. The thickness of the belt was estimated to be about 150 nm from the bending place of the belt, as shown in Fig. 3c. The microbelt–void–microbelt structure was also confirmed by the TEM image in Fig. 3e, in which one can see that the inner SnO_2 belt is hooped by the void space and the outer carbon shell. The inner SnO_2 consisted of numerous ultrafine SnO_2 nanoparticles about 10 nm in size. The enlarged edge of the belt showed that the thickness of the outer shell and void space were about 8 and 25 nm, respectively. The inset in Fig. 3e displays the diffraction rings of the sample, which can be readily indexed to the SnO_2 crystal plane of (110), (101), (200), *etc.* The HRTEM in Fig. 3f shows lattice spaces of 0.33 and 0.26 nm, which are consistent with the (110) and (101) planes of SnO_2. TEM elemental mapping technology was further utilized to analyze the edge of the belt, as shown in Fig. 3g–j. It can be seen that the Sn element is present in an uneven distribution and a small amount of tin can be observed in the dotted frame in Fig. 3g, which can be attributed to the fact that a small quantity of SnO_2 nanoparticles were anchored on a carbon microbelt in the synthesis process. The O, C, and N elements originating from carbonized polydopamine were uniformly distributed in the whole structure. The EDX spectrum demonstrated (Fig. S4†) that the atomic mass ratios of Sn, O, C, and N were 54.47, 27.72, 15.29, and 2.51 wt%, respectively. The nitrogen and oxygen on the carbon surface not only enhanced the reactivity and electric conductivity but also created lithium storage sites, which enhanced the capacity of the material. Fig. S5a and b† further show the specific surface area of the SnO_2 microbelts and microbelt–void–microbelt-structured SnO_2@C were 44.7 and 116.3 m^2 g^{-1}, and the corresponding

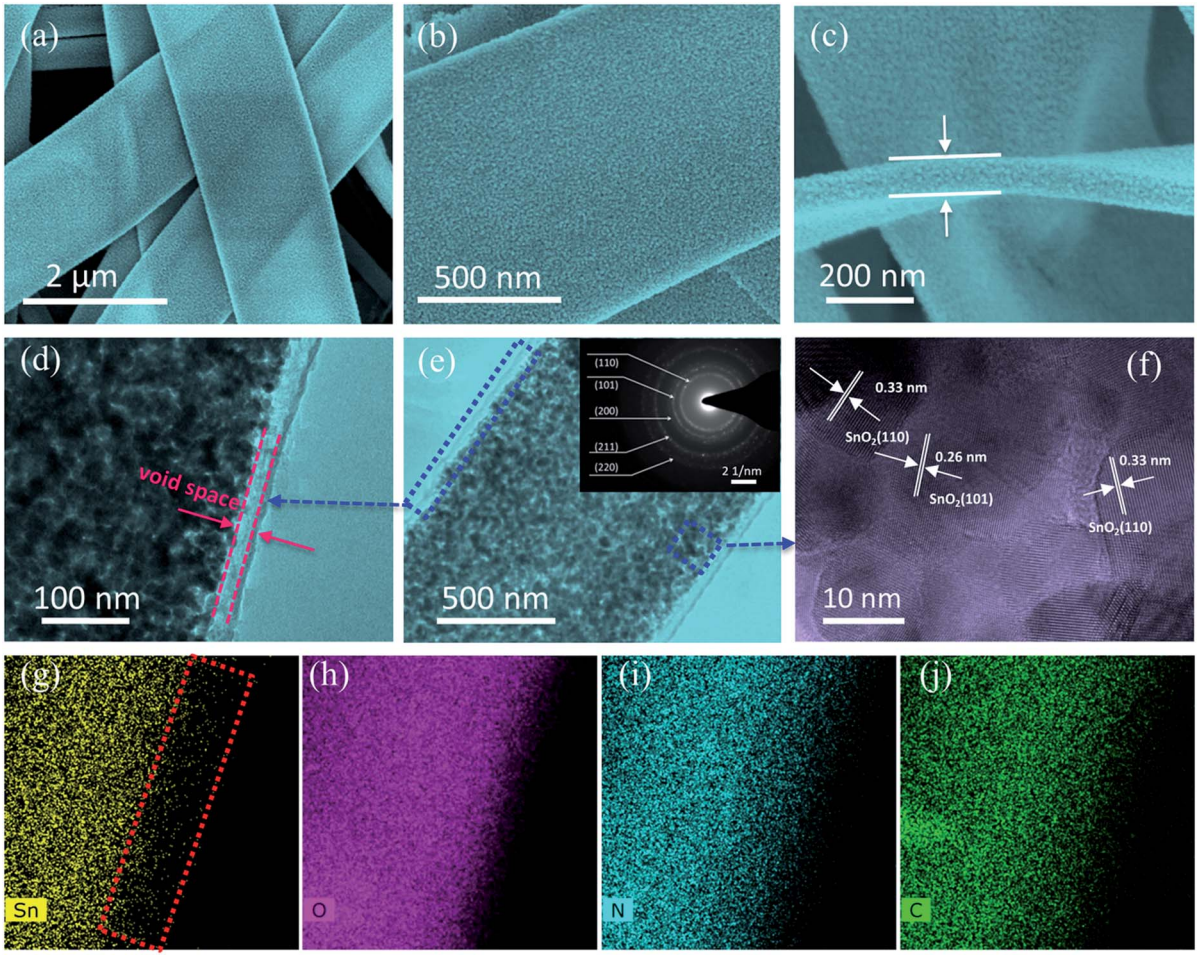

Fig. 3 Characterization of microbelt–void–microbelt-structured SnO_2@C. (a–c) SEM images, (d and e) TEM images and SAED patterns, while the inset of (e) and (f) show the HRTEM images, (g–j) the element mapping.

pore volumes were 0.17 and 0.26 $m^3\ g^{-1}$, respectively. The increased specific surface area and pore volume were induced by the void space, which buffer the volume changes in the electrochemical reaction.

To verify and highlight the advantages of the novel microbelt–void–microbelt design, we tested the microbelt–void–microbelt-structured SnO_2@C and pure SnO_2-electrode-based half-cells under the same conditions. Fig. 4a presents the initial 5 cyclic voltammograms (CVs) of the microbelt–void–microbelt-structured SnO_2@C-electrode-based half-cells at a scan rate of 0.2 mV s^{-1} and in a voltage window range from 0.02 to 3 V. In the first cathodic scan, a unique peak located at about 0.72 V revealed the lithiation of SnO_2 and the irreversible formation of an SEI (solid electrolyte interphase) layer. During the subsequent anodic scan process, the oxidation peak at about 0.55 V represented the delithiation reaction of Li_xSn: $Li_xSn \rightarrow Sn + xLi^+ + xe^-$ ($0 \leq x \leq 4.4$); the oxidation peak at about 1.3 V represented the formation of SnO: $Sn + Li_2O \rightarrow SnO + 2Li^+ + 2e^-$; the oxidation peak at about 1.9 V represented the formation of SnO_2:[67–70] $SnO + Li_2O \rightarrow SnO_2 + 2Li^+ + 2e^-$. In the cathodic scan process, the reduction peak at about 0.15 V represented the lithiation reaction of Sn: $Sn + xLi^+ + xe^- \rightarrow Li_xSn$ ($0 \leq x \leq 4.4$); also, the reduction peak at about 1.0 V represented the lithiation reaction of SnO_2: $SnO_2 + 4Li^+ + 4e^- \leftrightarrow Sn + 2Li_2O$. No obvious peaks of carbon were found in the CV measurement due to the fact that the present carbon had an amorphous structure under the relatively low carbonization temperature of 600 °C. These CV results demonstrated a highly reversible electrochemical reaction of the microbelt–void–microbelt-structured SnO_2@C sample.[71–74] Such a conclusion was further confirmed by the CV curves after 150 galvanostatic charge and discharge tests, as shown in Fig. 4b. It can be seen that the image demonstrates three oxidation peaks (at 0.5, 1.3, and 1.9 V), and two reduction peaks (at 0.2 and 1.0 V), proving that both the conversion reaction of SnO_2 to Sn and the Sn alloying reaction are highly reversible in the long-term electrochemical performance tests. Consequently, the whole electrochemical reactions of microbelt–void–microbelt-structured SnO_2@C electrode can be summarized as follows:

$$SnO_2 + 2Li^+ + 2e^- \leftrightarrow SnO + Li_2O,\ 356\ mA\ h\ g^{-1} \quad (1)$$

$$SnO + 2Li^+ + 2e^- \leftrightarrow Sn + Li_2O,\ 356\ mA\ h\ g^{-1} \quad (2)$$

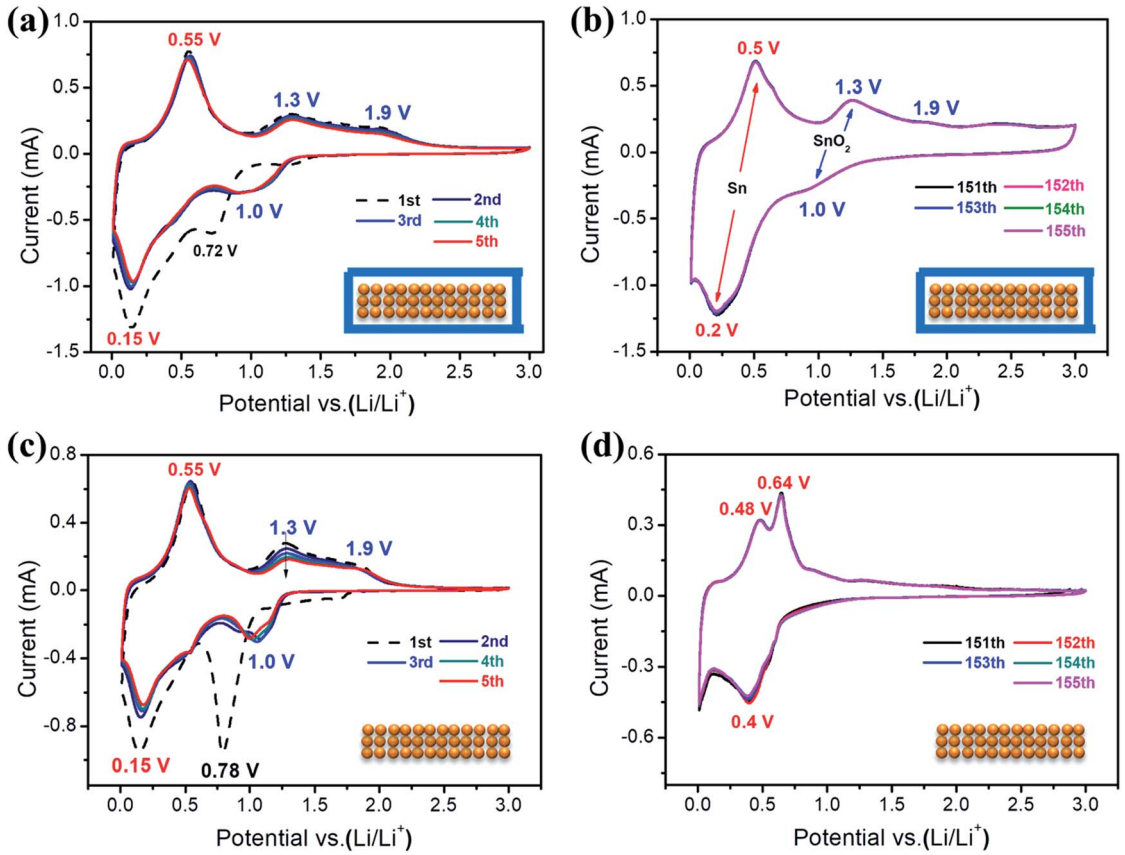

Fig. 4 CV curves of the two microbelt electrodes: (a) the initial 5 cycles and (b) after 150 galvanostatic charge and discharge tests of the microbelt–void–microbelt-structured SnO_2@C electrode. (c) The initial 5 cycles and (d) after 150 galvanostatic charge and discharge tests of the SnO_2 microbelts electrode.

$$Sn + xLi^+ + xe^- \leftrightarrow Li_xSn\ (0 \le x \le 4.4),\ 356\ mA\ h\ g^{-1} \quad (3)$$

Considering that the electrochemical reaction of SnO_2 to SnO, SnO to Sn, and Sn to $SnLi_x$ processes are all reversible, and the corresponding specific capacities are 356, 356, and 782 mA h g^{-1}, respectively, thus, the theoretical capacity of the present SnO_2 is the sum of these three parts, which is 1494 mA h g^{-1}.

For comparison, the initial 5 CV curves of the pure SnO_2 microbelt half-cell are recorded in Fig. 4c, which shows some obvious differences compared with the microbelt–void–microbelt-structured SnO_2@C electrode in Fig. 4a. First, the SEI layer formation peak (at about 0.78 V) is much stronger, which implies that the SnO_2 microbelt electrode suffers more irreversible electrolyte consumption and side reactions. In addition, the oxidation peaks ranging from 1.0–2.0 V show a significantly weakening trend, which proves that the conversion reaction of SnO_2 to Sn gradually becomes irreversible. Such a conclusion was also confirmed by the CV curves after 150 galvanostatic charge and discharge tests (Fig. 4d), in which the oxidation peaks at 1.0–2.0 V almost disappeared, and only Sn alloying and dealloying peaks were observed.

The detailed cycle capacities of the microbelt–void–microbelt-structured SnO_2@C and SnO_2 microbelts electrodes at 300 mA g^{-1} are shown in Fig. 5a. It can be seen that the microbelt–void–microbelt-structured SnO_2@C electrodes (red curve) underwent a slight capacity decay (967 mA h g^{-1} at the 44th cycle) in the initial cycles, while the electrode capacity increased to an outstanding high capacity of 1227 mA h g^{-1} after 300 cycles. For comparison, the pure SnO_2 microbelts electrodes (green curve) suffered from a continuous capacity decay and the corresponding reversible capacity was 608 mA h g^{-1} after 150 cycles and 425 mA h g^{-1} after 300 cycles.

We further tested the long cycling performance of the microbelt–void–microbelt-structured SnO_2@C electrode at 1.5 A g^{-1} after 300 cycles at 0.3 A g^{-1}. The electrode exhibited capacity fluctuations at large current density, and the corresponding capacity was 718 mA h g^{-1} at 500 cycles and 757 mA h g^{-1} at 1000 cycles, as shown in Fig. S6.† Moreover, the initial coulombic efficiencies for the microbelt–void–microbelt-structured SnO_2@C and pure SnO_2 microbelt were 70.3% and 64.3%, respectively. Furthermore, the coulombic efficiency for the microbelt–void–microbelt-structured SnO_2@C electrode was more than 98% after the first cycle, which was still higher than that of the SnO_2 microbelt electrode (91% at the second cycle). These coulombic efficiency tests results further proved that the electrochemical reaction of the microbelt–void–microbelt-structured SnO_2@C electrode was more reversible than that of the pure SnO_2 microbelt electrode.

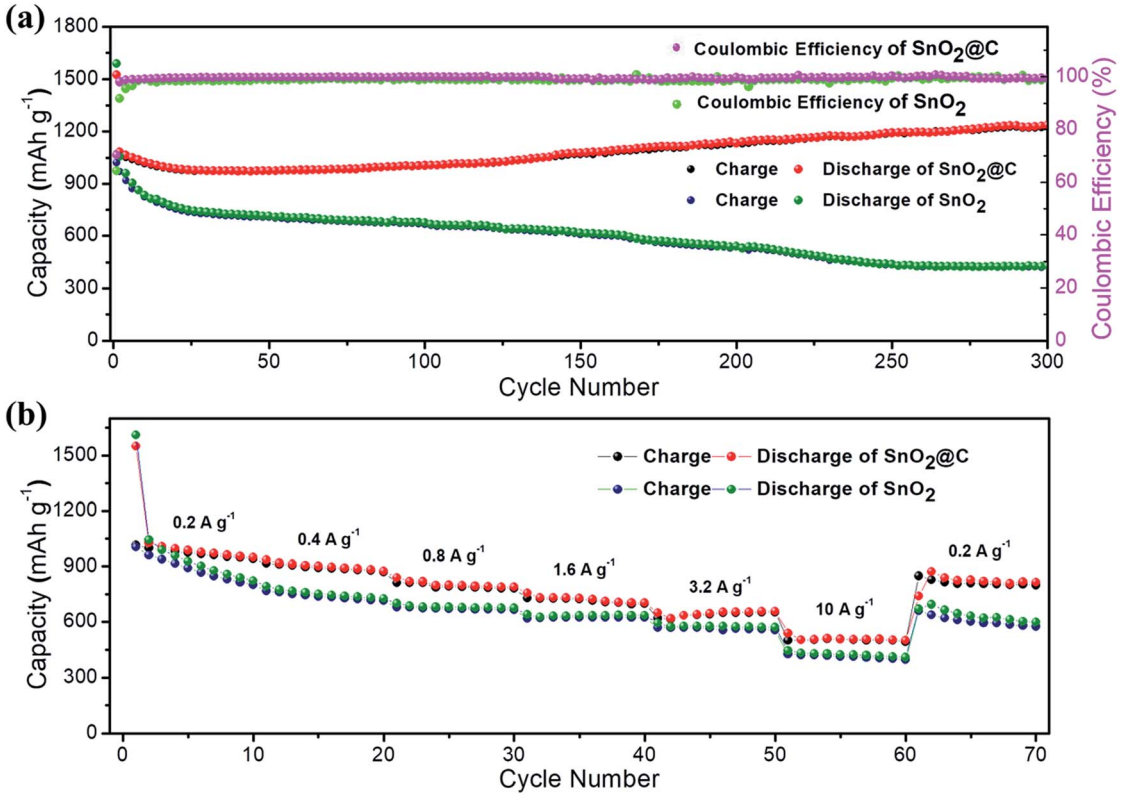

Fig. 5 (a) Cyclic performance and coulombic efficiency curves of microbelt–void–microbelt-structured SnO_2@C and SnO_2 microbelts-based half-cells. (b) Rate performance for the two microbelts-based half-cells.

Fig. 5b demonstrates the rate performance of the two electrodes. The microbelt–void–microbelt-structured SnO_2@C electrode exhibited a superior rate performance, and the corresponding capacities were 989, 904, 810, 726, 638, and 509 mA h g^{-1} at current densities of 0.2, 0.4, 0.8, 1.6, 3.2, and 10 A g^{-1}, respectively. For comparison, the SnO_2 microbelt electrode delivered lower reversible capacities of 938, 753, 676, 626, 569, and 420 mA h g^{-1} at the same current densities. The corresponding charge and discharge profiles of the two electrodes are shown in Figs S7a and b (see ESI†). Notably, the microbelt–void–microbelt-structured SnO_2@C electrode recovered a high reversible capacity of 814 mA h g^{-1}, while the SnO_2 electrode recovered a relatively low capacity of 622 mA h g^{-1}. Capacity and capacity retention rate *vs.* current density plots of the microbelt–void–microbelt-structured SnO_2@C and SnO_2 microbelts electrodes are shown in Fig. S8a and b.† From these images, we can clearly see that the microbelt–void–microbelt-structured SnO_2@C electrode material delivered superior rate performance under the variable cycling rates. These results further support the conclusion that the prepared microbelt–void–microbelt SnO_2@C electrode has the characteristic of an excellent rate performance.

Fig. 6a shows the initial 5 charge and discharge profiles of the microbelt–void–microbelt-structured SnO_2@C half-cell. The first discharge profile delivered a high capacity of 1590 mA h g^{-1}, which was caused by the reversible lithiation reaction of the microbelt–void–microbelt-structured SnO_2@C active materials, the irreversible formation of an SEI layer, and some inevitable side reactions. From the charge profiles, we can also see two obvious charging platforms at about 0.01–1.0 V and 1.0–2.0 V, which correspond to the delithiation of $SnLi_{4.4}$ and the conversion of Sn to SnO_2, respectively.

The two charging platforms for the 50th, 100th, 200th, 250th, and 300th cycles are also shown in Fig. 6b. Compared with Fig. 6a, the charging platform at 0.1–1.0 V almost overlaps in the whole process, while the charging platform at 1.0–2.0 V shows a decreasing trend and a capacity increase on this platform. To further investigate these phenomena, we characterized the cycled microbelt–void–microbelt-structured SnO_2@C sample. Fig. 6c and d show the XPS peaks of the cycled microbelt–void–microbelt-structured SnO_2@C sample. After electrochemical system cycling, the relative intensity of the C 1s, N 1s peak became weaker, while O 1s became stronger. In addition, F 1s appeared at about 686 eV after cycling. These phenomena can be attributed to the electrode material surface being covered by an SEI (solid electrolyte interphase) layer, which originates from the decomposition of the electrolyte (containing a lot of O and F elements). In addition, the Sn $3d_{3/2}$ and Sn $3d_{5/2}$ peaks could be clearly observed compared with such peaks before the cycle, which prove massively the existence of SnO_2 in the cycled sample. Thus, we could draw the conclusion that both the alloying reaction and conversion reaction contribute to the high capacity of the SnO_2@C microbelts electrode. After cycling, the microbelt–void–microbelt-structured SnO_2@C still kept the belt

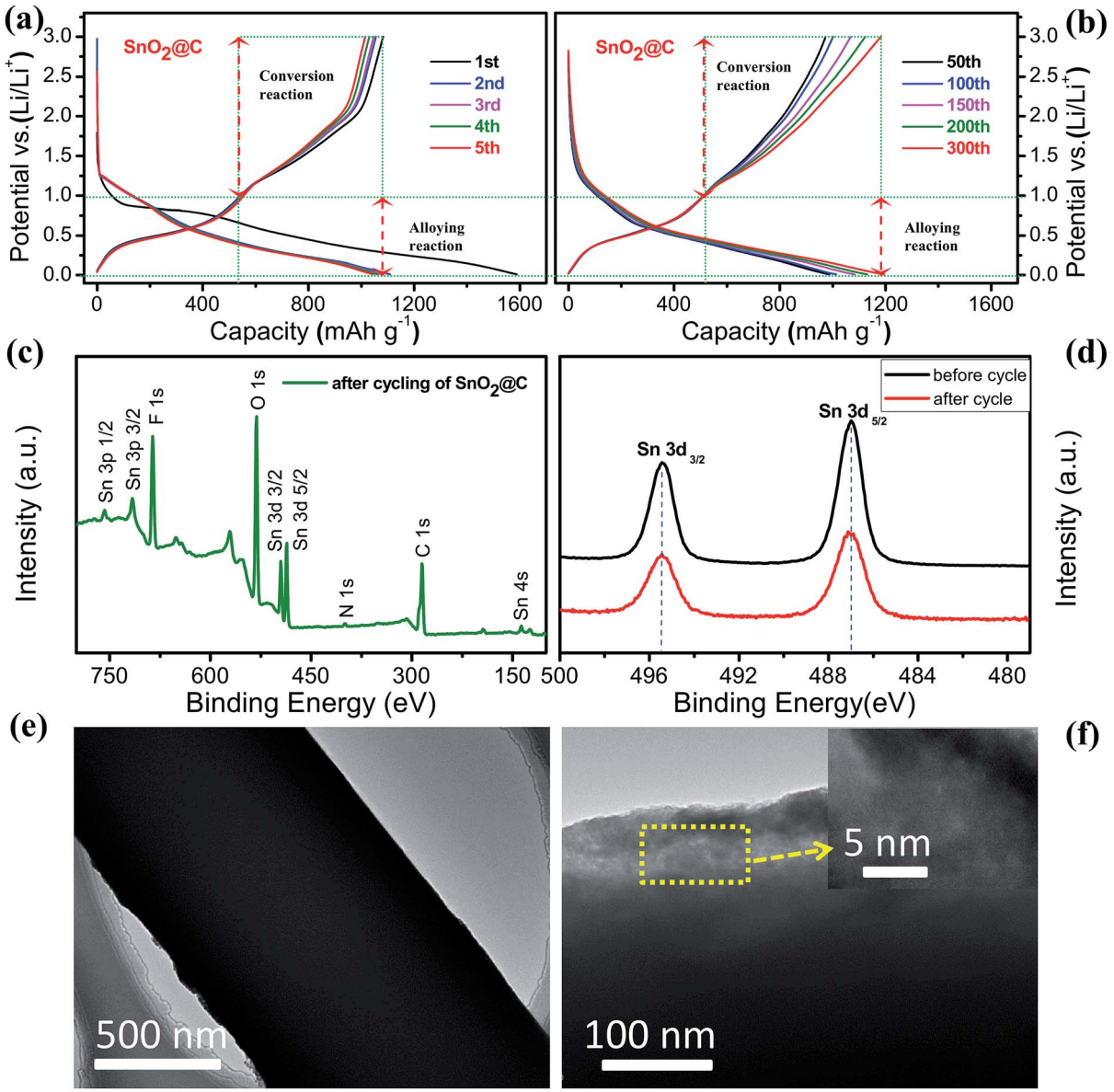

Fig. 6 (a) Galvanostatic discharge–charge profiles of the microbelt–void–microbelt-structured SnO_2@C electrode in the initial 5 cycles. (b) Typical galvanostatic discharge–charge profiles of the microbelt–void–microbelt-structured SnO_2@C electrode in the 50th, 100th, 200th, 250th, and 300th cycles. (c) Full XPS spectrum and (d) high-resolution Sn 3d XPS spectrum after the cyclic tests. (e and f) TEM images of the microbelt–void–microbelt-structured SnO_2@C electrode after the cyclic tests.

structure, as shown in Fig. 6e and f. However, the initial crystallized SnO_2 sample became amorphous and filled in the initial designed void space, thus the increasing capacity can be attributed to the fact that the amorphous active material benefits a short lithium ion diffusion distance and boosts the electrochemical reaction.[75] For comparison, we also drew the typical discharge–charge profiles for the SnO_2 microbelt electrode for the initial 5 cycles and for the 50th, 100th, 200th, 250th, and 300th cycles (Figs S9a and b, ESI†). It can be clearly seen that the platform caused by the conversion reaction gradually disappeared in the cycle process. Moreover, the Sn dealloying platform was elevated and the capacity also significantly attenuated, proving that the kinetics of the battery gradually improved during the cycling process.

To further prove the transport kinetics of electrons and ions facilitated by the designed microbelt–void–microbelt structure, electrochemical impedance spectroscopy (EIS) was conducted on the two microbelts half-cells under the same conditions. Before cycling, the measured EIS spectra in Fig. S10a† consisted of a semicircle in the high-to-medium frequency region and a straight line in the low frequency region, while the EIS spectra in Fig. S10b† shows two semicircles in the high-to-medium frequency region, and the extra semicircle is caused by the SEI layer after cycling. The corresponding equivalent circuit and calculated resistances of the microbelt–void–microbelt SnO_2@C microbelt cell are shown in Fig. S10c and d,† and the charge transfer resistances (R_{ct}) can be seen to be reduced from 84.8 to 66.7 Ω. For comparison, the R_{ct} of the pure SnO_2 microbelt cell

increased from 109.5 to 151.6 Ω. Therefore, these measurements verify that the microbelt–void space design improves the cell kinetics.

The present microbelt–void–microbelt-structured SnO_2@C electrode exhibited superior electrochemical lithium storage compared with recent published SnO_2 anode materials (Table 1),[22,46,76,77] whereby the enhanced performance can be explained as follows. First, the outer micro-scale length and width of the carbon belt with a nanoscale thickness shorted the lithium ion diffusion distance and favor fast electronic conduction, which improves the cell kinetics. Second, the inner SnO_2 microbelts consisting of numerous cross-linked ultrafine SnO_2 nanoparticles offer convenient channels for lithium ion diffusion. Third, due to the existence of the void space, the volume inflation of the active SnO_2 microbelts can be confined in the nanoscale thickness of the carbon shell, and thus perfectly solve the volume inflation problem. Benefitting from the rational design, both the Sn alloying reaction and SnO_2 conversion reaction are highly active and reversible during the cycling process, as verified by the CV measurements in Fig. 4 and the cycled XPS measurements in Fig. 6.

Finally, we further assembled microbelt–void–microbelt-structured SnO_2@C-anode-based full-cells coupled with a commercial $LiCoO_2$ cathode. The full-cells were tested in the voltage window range from 1.5–3.9 V, and for convenience, the current density and capacity of the cells were based on the mass of the microbelt–void–microbelt SnO_2@C. Fig. 7a presents the CV curves of the full-cells, in which a strong peak at about 3.4 V and a weak peak at about 2.6 V could be clearly observed in the cathodic scan. Such two discharge platforms were also confirmed by the discharge profiles, as shown in Fig. 7b. In addition, we also calculated the theoretical discharge platform to be 3.4 V and 2.6 V in Fig. 7c, respectively, which are consistent with the results of Fig. 7a and b. These results further demonstrate that the alloying and conversion of SnO_2 were reversible in the full-cells. Fig. 7d shows the cycle performance of the full-cell, where the reversible capacity was 588 mA h g^{-1} after 100 cycles. To demonstrate the practical application, an as-prepared $LiCoO_2$/microbelt–void–microbelt-structured SnO_2@C full-cell was applied to light 10 red and 10 yellow LEDs as shown in the inset of Fig. 7d, which further verified the SnO_2@C microbelt as a promising candidate as an anode material in the next-generation LIBs.

4. Conclusion

Microbelt–void–microbelt-structured SnO_2@C belts were engineered *via* a controllable and effective template method for the first time. The novel nanostructures, in which the ultrafine SnO_2 particles-derived microbelt was coated on a thin carbon shell with abundant void space, take full advantage of both a nanoparticles and microbelts strategy, rendering the high reactivity of SnO_2 when applied as an electrode material for LIBs. For the half-cell test, the microbelt–void–microbelt-structured SnO_2@C

Table 1 Comparison table of the present microbelt–void–microbelt-structured SnO_2@C with the recent published SnO_2 anodes

Electrode description	Current density (mA g^{-1})	Cycle number	Reversible capacity (mA h g^{-1})	Capacity retention (%)	High rate capability	Year of publication	Reference
Microbelt–void–microbelt-structured SnO_2@C	300	300	1070	114	509 mA h g^{-1} at 10 A g^{-1}	This work	This work
Textile-based SnO_2 ultra-flexible	85	100	969	90	656 mA h g^{-1} at 1.5 A g^{-1}	2019	78
SnO_2 anchored on nitrogen/sulfur codoped graphene	1000	500	893	99.2	698.3 mA h g^{-1} at 2 A g^{-1}	2018	79
Porous-SnO_2/rGO nanocomposite	78	150	885		262 mA h g^{-1} at 3.9 A g^{-1}	2018	80
SnO_2–Fe–graphite composites	200	150	940	100	720 mA h g^{-1} at 3.4 A g^{-1}	2017	81
Phosphorus covalently cross-linking SnO_2 and graphene	100	200	550	135	419 mA h g^{-1} at 1.0 A g^{-1}	2017	82
SnO_2/void@C nanofibers	200	200	986	80.3	284 mA h g^{-1} at 3.2 A g^{-1}	2016	83
Carbon-encapsulated porous SnO_2	50	120	871	71.4	409.6 mA h g^{-1} at 2.5 A g^{-1}	2016	84
N-doped carbon-coated SnO_2 submicroboxes	500	100	491		256 mA h g^{-1} at 5A g^{-1}	2016	85
Flexible SnO_2/N-doped carbon nanofiber films	1000	300	754	84.3	246 mA h g^{-1} at 10 A g^{-1}	2015	86
Carbon-coated $NiCo_2O_4$@SnO_2 nanostructures	100	100	654	60.4	348 mA h g^{-1} at 1 A g^{-1}	2015	87
Ordered network of interconnected SnO_2 nanoparticles	391	100	778	—	290 mA h g^{-1} at 4.7 A g^{-1}	2014	88
Bowl-like SnO_2@carbon hollow particles	400	100	963	79.7	850 mA h g^{-1} at 1.6 A g^{-1}	2014	89

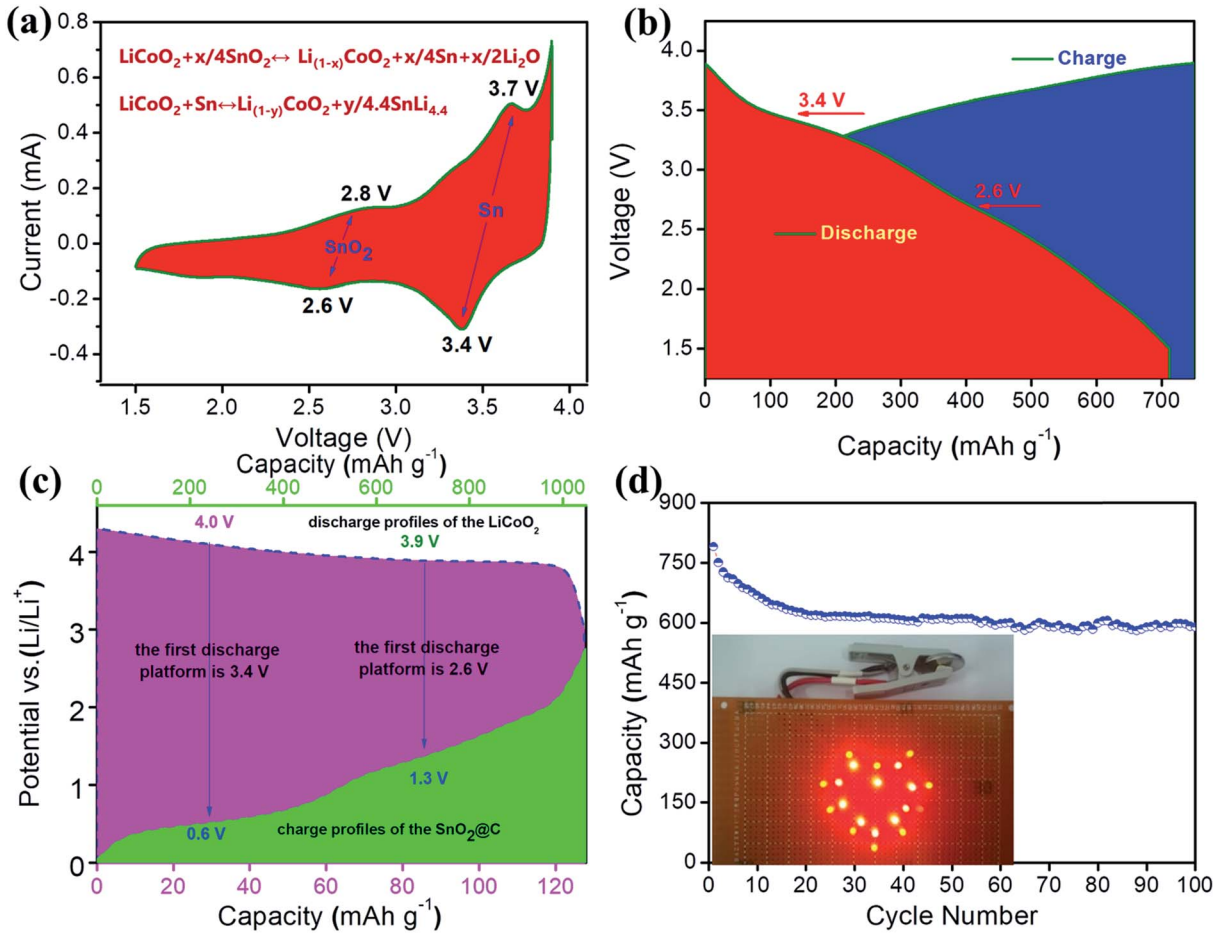

Fig. 7 (a) CV curves of the microbelt–void–microbelt-structured SnO_2@C/$LiCoO_2$-based full-cell. (b) Typical discharge–charge profiles. (c) Discharge ($LiCoO_2$ electrode in half-cell, upper) and charge (microbelt–void–microbelt-structured SnO_2@C electrode in half-cell, lower) curves. (d) Cycle performance of the full-cell.

electrode delivered a high capacity of 1227 mA h g^{-1} after 300 cycles at 300 mA g^{-1}, and a superior rate performance of 509 mA h g^{-1} under a high current density of 10 A g^{-1}. For the full-cell test, the capacity was 588 mA h g^{-1} after 100 cycles, and the conversion of SnO_2 to Sn was highly reversible for both the half- and full-cells. This work may promote the practical use of microbelt–void–microbelt-structured SnO_2@C materials.

Conflicts of interest

There are no conflicts to declare.

Acknowledgements

This project was financially supported by the National Natural Science Foundation of China (No. 61675175), Program Projects of Science and Technology Innovative Research Team of Henan Province (18IRTSTHN017), Key Research Projects of Henan Provincial Department of Education (17A140011), Science and Technology Project of Henan Province (182300410218) and Nanhu Scholars Program for Young Scholars of XYNU.

Notes and references

1 M. M. Thackeray, C. Wolverton and E. D. Isaacs, *Energy Environ. Sci.*, 2012, **5**, 7854–7863.
2 J. W. Choi and D. Aurbach, *Nat. Rev. Mater.*, 2016, **1**, 16013, DOI: 10.1038/natrevmats.2016.13.
3 S. Choi, T.-w. Kwon, A. Coskun and J. W. Choi, *Science*, 2017, **357**, 279–283.
4 P. Hou, H. Zhang, X. Deng, X. Xu and L. Zhang, *ACS Appl. Mater. Interfaces*, 2017, **9**, 29643–29653.
5 X. Sun, G.-P. Hao, X. Lu, L. Xi, B. Liu, W. Si, C. Ma, Q. Liu, Q. Zhang, S. Kaskel and O. G. Schmidt, *J. Mater. Chem. A*, 2016, **4**, 10166–10173.
6 X. Sun, W. Si, X. Liu, J. Deng, L. Xi, L. Liu, C. Yan and O. G. Schmidt, *Nano Energy*, 2014, **9**, 168–175.
7 D. Li, X. Li, X. Hou, X. Sun, B. Liu and D. He, *Chem. Commun.*, 2014, **50**, 9361–9364.
8 W. Tang, L. Liu, Y. Zhu, H. Sun, Y. Wu and K. Zhu, *Energy Environ. Sci.*, 2012, **5**, 6909–6913.
9 W. He, C. Wang, H. Li, X. Deng, X. Xu and T. Zhai, *Adv. Energy Mater.*, 2017, **7**, 242–250.

10 X. Sun, X. Lu, S. Huang, L. Xi, L. Liu, B. Liu, Q. Weng, L. Zhang and O. G. Schmidt, *ACS Appl. Mater. Interfaces*, 2017, **9**, 38556–38566.
11 X. Hou, S. Xue, M. Liu, X. Shang, Y. Fu and D. He, *Chem. Eng. J.*, 2018, **350**, 29–36.
12 P. Poizot, S. Laruelle, S. Grugeon, L. Dupont and J. M. Tarascon, *Nature*, 2000, **407**, 496–499.
13 D. Chao, C. Zhu, P. Yang, X. Xia, J. Liu, J. Wang, X. Fan, S. V. Savilov, J. Lin, H. J. Fan and Z. X. Shen, *Nat. Commun.*, 2016, **7**, 12122, DOI: 10.1038/ncomms12122.
14 W. Xie, S. Li, S. Wang, S. Xue, Z. Liu, X. Jiang and D. He, *ACS Appl. Mater. Interfaces*, 2014, **6**, 20334–20339.
15 C. Guan, X. Wang, Q. Zhang, Z. Fan, H. Zhang and H. J. Fan, *Nano Lett.*, 2014, **14**, 4852–4858.
16 X. Wang, L. Sun, R. Agung Susantyoko, Y. Fan and Q. Zhang, *Nano Energy*, 2014, **8**, 71–77.
17 X. Wang, Y. Fan, R. Agung Susantyoko, Q. Xiao, L. Sun, D. He and Q. Zhang, *Nano Energy*, 2014, **5**, 91–96.
18 S. Ni, P. Huang, D. Chao, G. Yuan, L. Zhang, F. Zhao and J. Li, *Adv. Funct. Mater.*, 2017, **27**, 1701808.
19 D. Liu, Z. j. Liu, X. Li, W. Xie, Q. Wang, Q. Liu, Y. Fu and D. He, *Small*, 2017, **13**, 1702000, DOI: 10.1002/smll.201702000.
20 S. Ni, X. Lv, J. Ma, X. Yang and L. Zhang, *J. Power Sources*, 2014, **248**, 122–129.
21 Y. Sun, X. Hu, W. Luo, F. Xia and Y. Huang, *Adv. Funct. Mater.*, 2012, **23**, 2436–2444.
22 K. Zhao, L. Zhang, R. Xia, Y. Dong, W. Xu, C. Niu, L. He, M. Yan, L. Qu and L. Mai, *Small*, 2015, **12**, 588–594.
23 Y. Wang, Y. Wang, D. Jia, Z. Peng, Y. Xia and G. Zheng, *Nano Lett.*, 2014, **14**, 1080–1084.
24 L. Liu, Y. Hou, J. Wang, J. Chen, H.-K. Liu, Y. Wu and J. Wang, *Adv. Mater. Interfaces*, 2016, **3**, 1600030.
25 X. Wang, H.-M. Kim, Y. Xiao and Y.-K. Sun, *J. Mater. Chem. A*, 2016, **4**, 14915–14931.
26 W. Li, H. Li, Z. Lu, L. Gan, L. Ke, T. Zhai and H. Zhou, *Energy Environ. Sci.*, 2015, **8**, 3629–3636.
27 Y. Chen, X. Li, K. Park, L. Zhou, H. Huang, Y.-W. Mai and B. Goodenough John, *Angew. Chem., Int. Ed.*, 2016, **55**, 15831–15834.
28 S. Ni, B. Zheng, J. Liu, D. Chao, X. Yang, Z. Shen and J. Zhao, *J. Mater. Chem. A*, 2018, **6**, 18821–18826.
29 S. Ni, J. Liu, D. Chao and L. Mai, *Adv. Energy Mater.*, 2019, 1803324.
30 H. Wang, X. Jiang, Y. Chai, X. Yang and R. Yuan, *J. Power Sources*, 2018, **379**, 191–196.
31 J. Liang, X.-Y. Yu, H. Zhou, B. Wu Hao, S. Ding and W. Lou Xiong, *Angew. Chem., Int. Ed.*, 2014, **53**, 12803–12807.
32 B. Huang, X. Li, Y. Pei, S. Li, X. Cao, C. Massé Robert and G. Cao, *Small*, 2016, **12**, 1945–1955.
33 Y. Yang, X. Zhao, H.-E. Wang, M. Li, C. Hao, M. Ji, S. Ren and G. Cao, *J. Mater. Chem. A*, 2018, **6**, 3479–3487.
34 X. Li, X. Meng, J. Liu, D. Geng, Y. Zhang, N. Banis Mohammad, Y. Li, J. Yang, R. Li, X. Sun, M. Cai and W. Verbrugge Mark, *Adv. Funct. Mater.*, 2012, **22**, 1647–1654.
35 Q. Wang, J. Xu, G. Shen, Y. Guo, X. Zhao, Y. Xia, H. Sun, P. Hou, W. Xie and X. Xu, *Electrochim. Acta*, 2019, **297**, 879–887.
36 S. Abouali, M. A. Garakani and J.-K. Kim, *Electrochim. Acta*, 2018, **284**, 436–443.
37 X. W. Lou, Y. Wang, C. Yuan, J. Y. Lee and L. A. Archer, *Adv. Mater.*, 2006, **18**, 2325–2329.
38 S.-M. Paek, E. Yoo and I. Honma, *Nano Lett.*, 2009, **9**, 72–75.
39 S. Chen Jun and W. Lou Xiong, *Small*, 2013, **9**, 1877–1893.
40 Q.-G. Shao, W.-M. Chen, Z.-H. Wang, L. Qie, L.-X. Yuan, W.-X. Zhang, X.-L. Hu and Y.-H. Huang, *Electrochem. Commun.*, 2011, **13**, 1431–1434.
41 G. Gao, B. Wu Hao, S. Ding and W. Lou Xiong, *Small*, 2014, **11**, 432–436.
42 M. Zhang, T. Wang and G. Cao, *Int. Mater. Rev.*, 2015, **60**, 330–352.
43 P. Manjula, R. Boppella and S. V. Manorama, *ACS Appl. Mater. Interfaces*, 2012, **4**, 6252–6260.
44 C. Miao, M. Liu, Y.-B. He, X. Qin, L. Tang, B. Huang, R. Li, B. Li and F. Kang, *Energy Storage Mater.*, 2016, **3**, 98–105.
45 Q. Liu, Y. Dou, B. Ruan, Z. Sun, S.-L. Chou and X. Dou Shi, *Chem. - Eur. J.*, 2016, **22**, 5853–5857.
46 C. Wang, G. Du, K. Ståhl, H. Huang, Y. Zhong and J. Z. Jiang, *J. Phys. Chem. C*, 2012, **116**, 4000–4011.
47 Z. Yang, S. Zhao, W. Jiang, X. Sun, Y. Meng, C. Sun and S. Ding, *Electrochim. Acta*, 2015, **158**, 321–326.
48 X. Zhang, J. Liang, G. Gao, S. Ding, Z. Yang, W. Yu and B. Q. Li, *Electrochim. Acta*, 2013, **98**, 263–267.
49 Z. Zhang, L. Wang, J. Xiao, F. Xiao and S. Wang, *ACS Appl. Mater. Interfaces*, 2015, **7**, 17963–17968.
50 Y. Zhu, H. Guo, H. Zhai and C. Cao, *ACS Appl. Mater. Interfaces*, 2015, **7**, 2745–2753.
51 X. Zhang, B. Jiang, J. Guo, Y. Xie and L. Tang, *J. Power Sources*, 2014, **268**, 365–371.
52 H. Z. Li, L. Y. Yang, J. Liu, S. T. Li, L. B. Fang, Y. K. Lu, H. R. Yang, S. L. Liu and M. Lei, *J. Power Sources*, 2016, **324**, 780–787.
53 X. Wang, X. Cao, L. Bourgeois, H. Guan, S. Chen, Y. Zhong, D.-M. Tang, H. Li, T. Zhai, L. Li, Y. Bando and D. Golberg, *Adv. Funct. Mater.*, 2012, **22**, 2682–2690.
54 N. Liu, H. Wu, M. T. McDowell, Y. Yao, C. Wang and Y. Cui, *Nano Lett.*, 2012, **12**, 3315–3321.
55 Y. J. Hong, M. Y. Son and Y. C. Kang, *Adv. Mater.*, 2013, **25**, 2279–2283.
56 J. Wang, W. Li, F. Wang, Y. Xia, A. M. Asiri and D. Zhao, *Nanoscale*, 2014, **6**, 3217–3222.
57 S. H. Choi and Y. C. Kang, *Chem. - Eur. J.*, 2014, **20**, 5835–5839.
58 J. Hong Young, Y. Son Mun and C. Kang Yun, *Adv. Mater.*, 2013, **25**, 2279–2283.
59 R. Zhao, X. Shen, Q. Wu, X. Zhang, W. Li, G. Gao, L. Zhu, L. Ni, G. Diao and M. Chen, *ACS Appl. Mater. Interfaces*, 2017, **9**, 24662–24670.
60 Z. Cai, L. Xu, M. Yan, C. Han, L. He, K. M. Hercule, C. Niu, Z. Yuan, W. Xu, L. Qu, K. Zhao and L. Mai, *Nano Lett.*, 2015, **15**, 738–744.
61 R. Purbia and S. Paria, *Nanoscale*, 2015, **7**, 19789–19873.

62 S. Koombhongse, W. Liu and D. H. Reneker, *J. Polym. Sci., Part B: Polym. Phys.*, 2001, **39**, 2598–2606.
63 S. Hwan Oh, J.-S. Park, M. Su Jo, Y. C. Kang and J. S. Cho, *Chem. Eng. J.*, 2018, **347**, 889–899.
64 H. Lee, S. M. Dellatore, W. M. Miller and P. B. Messersmith, *Science*, 2007, **318**, 426.
65 A. H. Ashok, T. R. Marques, S. Jauhar, M. M. Nour, G. M. Goodwin, A. H. Young and O. D. Howes, *Mol. Psychiatry*, 2017, **22**, 666.
66 H. Jiang, D. Ren, H. Wang, Y. Hu, S. Guo, H. Yuan, P. Hu, L. Zhang and C. Li, *Adv. Mater.*, 2015, **27**, 3687–3695.
67 H.-P. Cong, S. Xin and S.-H. Yu, *Nano Energy*, 2015, **13**, 482–490.
68 V. Etacheri, A. Seisenbaeva Gulaim, J. Caruthers, G. Daniel, J.-M. Nedelec, G. Kessler Vadim and G. Pol Vilas, *Adv. Energy Mater.*, 2014, **5**, 1401289.
69 S. Böhme, B. Philippe, K. Edström and L. Nyholm, *J. Phys. Chem. C*, 2017, **121**, 4924–4936.
70 Y. Zhang, Q. Xiao, G. Lei, Z. Li and X. Li, *Electrochim. Acta*, 2015, **178**, 336–343.
71 R. Wang, C. Xu, J. Sun, L. Gao and H. Yao, *ACS Appl. Mater. Interfaces*, 2014, **6**, 3427–3436.
72 R. Jia, J. Yue, Q. Xia, J. Xu, X. Zhu, S. Sun, T. Zhai and H. Xia, *Energy Storage Mater.*, 2018, **13**, 303–311.
73 S. Wang, L. Shi, G. Chen, C. Ba, Z. Wang, J. Zhu, Y. Zhao, M. Zhang and S. Yuan, *ACS Appl. Mater. Interfaces*, 2017, **9**, 17163–17171.
74 R. Hu, H. Zhang, Z. Lu, J. Liu, M. Zeng, L. Yang, B. Yuan and M. Zhu, *Nano Energy*, 2018, **45**, 255–265.
75 X. Jin, H. Huang, A. Wu, S. Gao, M. Lei, J. Zhao, X. Gao and G. Cao, *ACS Nano*, 2018, **12**, 8037–8047.
76 W.-S. Kim, Y. Hwa, J.-H. Jeun, H.-J. Sohn and S.-H. Hong, *J. Power Sources*, 2013, **225**, 108–112.
77 J. S. Chen and X. W. Lou, *Small*, 2013, **9**, 1877–1893.
78 X. Min, B. Sun, S. Chen, M. Fang, X. Wu, Y. g. Liu, A. Abdelkader, Z. Huang, T. Liu, K. Xi and R. Vasant Kumar, *Energy Storage Mater.*, 2019, **16**, 597–606.
79 H.-g. Wang, Q. Wu, Y. Wang, X. Wang, L. Wu, S. Song and H. Zhang, *Adv. Energy Mater.*, 2018, **0**, 1802993.
80 Q. Zhang, Q. Gao, W. Qian, H. Zhang, Z. Li, Y. Tan and W. Tian, *ChemistrySelect*, 2018, **3**, 4303–4309.
81 R. Hu, Y. Ouyang, T. Liang, H. Wang, J. Liu, J. Chen, C. Yang, L. Yang and M. Zhu, *Adv. Mater.*, 2017, **29**, 1605006.
82 L. Zhang, K. Zhao, R. Yu, M. Yan, W. Xu, Y. Dong, W. Ren, X. Xu, C. Tang and L. Mai, *Small*, 2017, **13**, 1603973.
83 W. Xie, L. Gu, F. Xia, B. Liu, X. Hou, Q. Wang, D. Liu and D. He, *J. Power Sources*, 2016, **327**, 21–28.
84 B. Huang, X. Li, Y. Pei, S. Li, X. Cao, R. C. Massé and G. Cao, *Small*, 2016, **12**, 1945–1955.
85 X. Zhou, L. Yu and X. W. Lou, *Adv. Energy Mater.*, 2016, **6**, 1600451.
86 L. Xia, S. Wang, G. Liu, L. Ding, D. Li, H. Wang and S. Qiao, *Small*, 2016, **12**, 853–859.
87 G. Gao, H. B. Wu, S. Ding and X. W. Lou, *Small*, 2015, **11**, 432–436.
88 V. Etacheri, G. A. Seisenbaeva, J. Caruthers, G. Daniel, J.-M. Nedelec, V. G. Kessler and V. G. Pol, *Adv. Energy Mater.*, 2015, **5**, 1401289.
89 J. Liang, X.-Y. Yu, H. Zhou, H. B. Wu, S. Ding and X. W. Lou, *Angew. Chem., Int. Ed.*, 2014, **53**, 12803–12807.